VSP

Advanced Composite Materials 18 (2009) 233–249

ADVANCED COMPOSITE MATERIALS
www.brill.nl/acm

Failure Pressure Prediction of Composite Cylinders for Hydrogen Storage Using Thermo-mechanical Analysis and Neural Network

J. Hu [a], **S. Sundararaman** [a], **V. G. K. Menta** [a], **K. Chandrashekhara** [a,*] **and William Chernicoff** [b]

[a] Department of Mechanical and Aerospace Engineering, Missouri University of Science and Technology, Rolla, MO 65409, USA

[b] US Department of Transportation, Washington, DC 20509, USA

Received 13 February 2008; accepted 26 July 2008

Abstract

Safe installation and operation of high-pressure composite cylinders for hydrogen storage are of primary concern. It is unavoidable for the cylinders to experience temperature variation and significant thermal input during service. The maximum failure pressure that the cylinder can sustain is affected due to the dependence of composite material properties on temperature and complexity of cylinder design. Most of the analysis reported for high-pressure composite cylinders is based on simplifying assumptions and does not account for complexities like thermo-mechanical behavior and temperature dependent material properties. In the present work, a comprehensive finite element simulation tool for the design of hydrogen storage cylinder system is developed. The structural response of the cylinder is analyzed using laminated shell theory accounting for transverse shear deformation and geometric nonlinearity. A composite failure model is used to evaluate the failure pressure under various thermo-mechanical loadings. A back-propagation neural network (NNk) model is developed to predict the maximum failure pressure using the analysis results. The failure pressures predicted from NNk model are compared with those from test cases. The developed NNk model is capable of predicting the failure pressure for any given loading condition.

Keywords

Composite cylinder, hydrogen storage, finite element analysis, neural network

1. Introduction

Composite high-pressure cylinders have potential application as hydrogen storage systems in automotives, transportation and stationary/portable storage systems due to their light weight, simplicity of the storage and low cost for storage and trans-

* To whom correspondence should be addressed. E-mail: chandra@mst.edu

Edited by JSCM and KSCM

DOI:10.1163/156855109X428790

port of hydrogen gas [1]. Typically, a composite high-pressure cylinder constitutes a high molecular weight polymer or aluminum liner that serves as a hydrogen gas permeation barrier. A filament-wound, carbon/epoxy composite laminate overwrapped outside the liner provides the desired pressure load bearing capacity [2]. A vehicle fuel system cylinder is capable of sustaining pressures of 34.5 MPa or higher by taking advantage of high modulus, high strength and low specific weight of modern high performance composite. In addition, the maturation of the filament winding manufacturing process further lowers the price to practical and common usage in mass transportation systems.

To design composite high-pressure cylinders with the highest possible safety, reliability and minimum weight considerations, the behavior of composite structures under various mechanical and thermal loadings need to be well understood. Studies have been conducted by various researchers [3–6] on the structure of composite hydrogen storage cylinder under mechanical loadings. Using the finite element method as a numerical tool, numerous studies have been conducted on high-pressure storage cylinders [7–9]. Compared to pure mechanical loading, fewer studies have been conducted on composite hydrogen storage cylinders subjected to thermal loads and combined thermo-mechanical loads [10–12].

In the present study, a thermo-mechanical finite element model has been developed for the analysis of hydrogen storage cylinders. The composite laminate wall of the hydrogen storage cylinder typically consists of helical laminated layers and hoop laminated layers. Both these layers along with an aluminum liner are considered for the analysis. During service, composite hydrogen storage cylinders unavoidably experience various thermal loadings combined with high pressure. To account for the working temperature variation in service, uniform temperature loadings ranging from 25°C to 140°C are considered for the analysis. Temperatures higher than 140°C are not considered in the present study as the composite matrix begins to burn at these temperatures. During the gas filling process, the inner temperature can increase up to around 100°C [11]. Hence, non-uniform thermal loadings have also been included in the study. The variation of material properties with temperature is significant for most composites. A temperature dependent material model has been developed and implemented in commercial finite element code ABAQUS, using user subroutines. A laminated shell theory [13, 14] accounting for out-of-plane shear strains and geometric nonlinearity is used for the analysis.

Considering various combinations of thermal loadings, winding angles and lamina stacking sequences in the analysis, to optimize the cylinder design and predict maximum failure pressure through case-by-case simulation, is a tremendous task. Therefore, a back-propagation neural network (NNk) model is developed to predict the failure pressure using the results from a few typical finite element simulation cases. The training process consists of training the network with three sets of simulation results with various winding angles and thermal loadings. Once trained, the developed NNk model can be used for guidance and optimization of hydrogen cylinder design. Some test cases, which are not included in the training sets, are uti-

lized to compare the predicted failure pressure from NNk model. A good agreement is found between failure pressures of the test cases with the NNk model.

2. Shear Deformable Shell Theory

A schematic of a hydrogen composite cylinder wall is shown in Fig. 1. The inner liner is made of aluminum that serves as a hydrogen gas permeation barrier. A filament-wound, carbon/epoxy composite laminate over-wrapped outside of the liner provides the desired pressure load bearing capacity [15]. In many current designs, a glass/epoxy layer is placed over the carbon/epoxy laminate to provide impact and damage resistance. The doubly curved shell theory accounting for out of plane shear deformations and geometric nonlinearity is used for the analysis of composite hydrogen storage cylinders.

A multilayered doubly curved shell in a curvilinear coordinate system $\{\xi_1, \xi_2, \zeta\}$ is shown in Fig. 2. The coordinates ξ_1 and ξ_2 specify the position on the middle

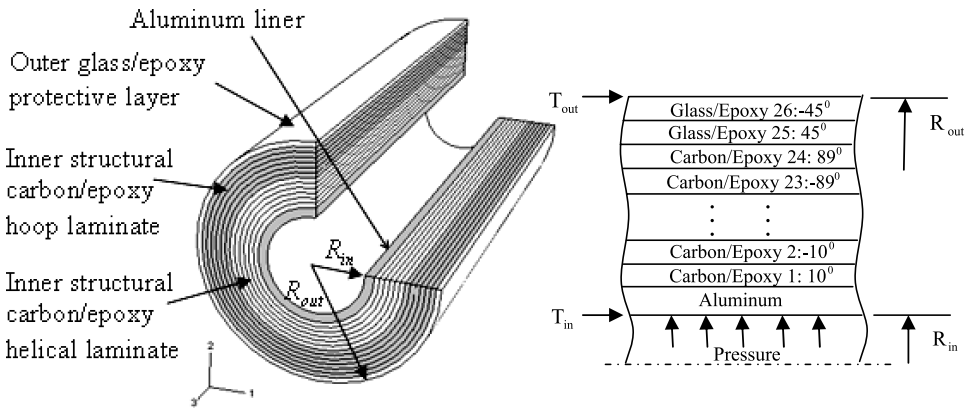

Figure 1. Structure scheme of hydrogen storage cylinder.

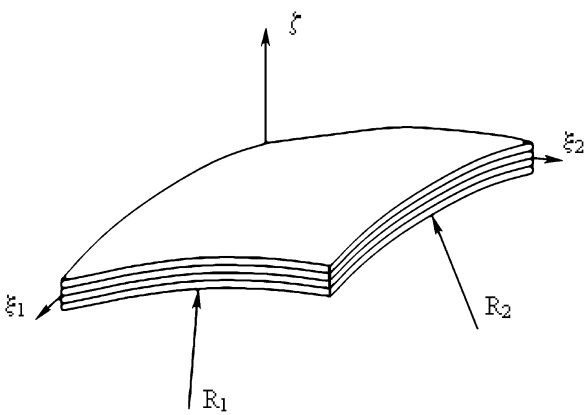

Figure 2. Doubly curved shell and coordinate system.

surface, while ζ measures the distance, along the outward normal, from the mid-surface to arbitrary point on the shell. The displacement field can be expressed as:

$$u(\xi_1, \xi_2, \zeta) = \left(1 + \frac{\zeta}{R_1}\right) u_0(\xi_1, \xi_2) + \zeta \phi_1(\xi_1, \xi_2), \tag{1a}$$

$$v(\xi_1, \xi_2, \zeta) = \left(1 + \frac{\zeta}{R_2}\right) v_0(\xi_1, \xi_2) + \zeta \phi_2(\xi_1, \xi_2), \tag{1b}$$

$$w(\xi_1, \xi_2, \zeta) = w_0(\xi_1, \xi_2). \tag{1c}$$

The nonlinear strain–displacement relations based on Sanders's shell theory are given as:

$$\begin{aligned} &\varepsilon_x = \varepsilon_x^0 + \zeta \kappa_x, && \varepsilon_y = \varepsilon_y^0 + \zeta \kappa_y, \\ &\gamma_{xy} = \gamma_{xy}^0 + \zeta \kappa_{xy}, && \gamma_{yz} = \gamma_{yz}^0, \qquad \gamma_{xz} = \gamma_{xz}^0, \end{aligned} \tag{2}$$

where ε_j^0 and κ_j are defined as:

$$\begin{aligned} &\varepsilon_x^0 = \frac{1}{\alpha_1}\frac{\partial u_0}{\partial \xi_1} + \frac{w_0}{R_1} + \frac{1}{2\alpha_1^2}\left(\frac{\partial w_0}{\partial \xi_1}\right)^2, && \kappa_x = \frac{1}{\alpha_1}\frac{\partial \phi_1}{\partial \xi_1}, \\ &\varepsilon_y^0 = \frac{1}{\alpha_2}\frac{\partial v_0}{\partial \xi_2} + \frac{w_0}{R_2} + \frac{1}{2\alpha_2^2}\left(\frac{\partial w_0}{\partial \xi_2}\right)^2, && \kappa_y = \frac{1}{\alpha_2}\frac{\partial \phi_2}{\partial \xi_2}, \\ &\gamma_{xy}^0 = \frac{1}{\alpha_1}\frac{\partial v_0}{\partial \xi_1} + \frac{1}{\alpha_2}\frac{\partial u_0}{\partial \xi_2} + \frac{1}{2\alpha_1\alpha_2}\frac{\partial w_0}{\partial \xi_1}\frac{\partial w_0}{\partial \xi_2}, && \gamma_{yz}^0 = \frac{1}{\alpha_2}\frac{\partial w_0}{\partial \xi_2} + \phi_2 - \frac{v_0}{R_2}, \\ &\gamma_{xz}^0 = \frac{1}{\alpha_1}\frac{\partial w_0}{\partial \xi_1} + \phi_1 - \frac{u_0}{R_1}, \\ &\kappa_{xy} = \frac{1}{\alpha_1}\frac{\partial \phi_2}{\partial \xi_1} + \frac{1}{\alpha_2}\frac{\partial \phi_1}{\partial \xi_2} - c_0\left(\frac{1}{\alpha_1}\frac{\partial v_0}{\partial \xi_1} - \frac{1}{\alpha_2}\frac{\partial u_0}{\partial \xi_2}\right), \\ &c_0 = \frac{1}{2}\left(\frac{1}{R_1} - \frac{1}{R_2}\right), \qquad \mathrm{d}x = \alpha_1\,\mathrm{d}\xi_1, \qquad \mathrm{d}y = \alpha_2\,\mathrm{d}\xi_2. \end{aligned} \tag{3}$$

In equation (3), u and v are the displacements in the direction of the tangents to the coordinate lines ξ_1 and ξ_2, respectively, w is the displacement in the direction of the outward normal, R_1, R_2 are the radii of curvature of the shell and ϕ_1, ϕ_2 are the rotations.

The stress–strain relation, accounting for thermal effects, in the shell coordinates for a kth layer can be expressed as [14]:

$$\begin{Bmatrix} \sigma_x \\ \sigma_y \\ \tau_{xy} \\ \tau_{yz} \\ \tau_{xz} \end{Bmatrix}_k = \begin{bmatrix} Q_{11} & Q_{12} & Q_{16} & 0 & 0 \\ Q_{12} & Q_{22} & Q_{26} & 0 & 0 \\ Q_{16} & Q_{26} & Q_{66} & 0 & 0 \\ 0 & 0 & 0 & Q_{44} & Q_{45} \\ 0 & 0 & 0 & Q_{45} & Q_{55} \end{bmatrix}_k \begin{Bmatrix} \varepsilon_x - \alpha_x T \\ \varepsilon_y - \alpha_y T \\ \gamma_{xy} - \alpha_{xy} T \\ \gamma_{yz} \\ \gamma_{xz} \end{Bmatrix}_k, \tag{4}$$

where Q_{ij} are the transformed elastic coefficients, T is the given temperature distribution, $(\alpha_x, \alpha_y, \alpha_{xy})$ are the thermal expansion coefficients in the shell coordinates. It should be noted that the out-of-plane normal stress (σ_z) is neglected in comparison with in-plane normal stresses (σ_x and σ_y).

The laminate constitutive equations can be obtained by integrating equation (4) over the thickness, and are given by:

$$\begin{Bmatrix} N_x \\ N_y \\ N_{xy} \\ Q_{xz} \\ Q_{yz} \\ M_x \\ M_y \\ M_{xy} \end{Bmatrix} = \begin{bmatrix} A_{11} & A_{12} & A_{16} & 0 & 0 & B_{11} & B_{12} & B_{16} \\ A_{12} & A_{22} & A_{26} & 0 & 0 & B_{12} & B_{22} & B_{26} \\ A_{16} & A_{26} & A_{66} & 0 & 0 & B_{16} & B_{26} & B_{66} \\ 0 & 0 & 0 & A_{44} & A_{45} & 0 & 0 & 0 \\ 0 & 0 & 0 & A_{45} & A_{55} & 0 & 0 & 0 \\ B_{11} & B_{12} & B_{16} & 0 & 0 & D_{11} & D_{12} & D_{16} \\ B_{12} & B_{22} & B_{26} & 0 & 0 & D_{12} & D_{22} & D_{26} \\ B_{16} & B_{26} & B_{66} & 0 & 0 & D_{16} & D_{26} & D_{66} \end{bmatrix} \times \begin{Bmatrix} \varepsilon_x^0 \\ \varepsilon_y^0 \\ \gamma_{xy}^0 \\ \gamma_{xz}^0 \\ \gamma_{yz}^0 \\ \kappa_x \\ \kappa_y \\ \kappa_{xy} \end{Bmatrix} - \begin{Bmatrix} N_x^T \\ N_y^T \\ N_{xy}^T \\ 0 \\ 0 \\ M_x^T \\ M_y^T \\ M_{xy}^T \end{Bmatrix}, \tag{5}$$

where N^T and M^T are thermal stress and moment resultants and are given by

$$\begin{Bmatrix} N_x^T & M_x^T \\ N_y^T & M_y^T \\ N_{xy}^T & M_{xy}^T \end{Bmatrix} = \int_{-h/2}^{h/2} \begin{bmatrix} Q_{11} & Q_{12} & Q_{16} \\ Q_{12} & Q_{22} & Q_{26} \\ Q_{16} & Q_{26} & Q_{66} \end{bmatrix} \begin{Bmatrix} \alpha_x \\ \alpha_y \\ \alpha_{xy} \end{Bmatrix} (1 \;\; z) T \, \mathrm{d}z. \tag{6a}$$

The stiffness coefficients in equation (5) are defined as:

$$(A_{ij} \quad B_{ij} \quad D_{ij}) = \int_{-h/2}^{h/2} Q_{ij} (1 \;\; z \;\; z^2) \, \mathrm{d}z \quad (i, j = 1, 2, 6), \tag{6b}$$

$$A_{ij} = \int_{-h/2}^{h/2} K_i K_j Q_{ij} \, \mathrm{d}z \quad (i, j = 4, 5), \tag{6c}$$

where K is shear correction factor.

Following the standard finite element procedure, the generalized displacements in any element are given by:

$$\Delta = \begin{Bmatrix} u \\ v \\ w \\ \phi_1 \\ \phi_2 \end{Bmatrix} = \sum_{i=1}^{N} \begin{Bmatrix} u \\ v \\ w \\ \phi_1 \\ \phi_2 \end{Bmatrix}_i \psi_i, \tag{7}$$

where N is the number of nodes in the element and ψ_i are the interpolation functions. Substituting equation (7) in equation (3), the strains can be expressed as:

$$\varepsilon = B_1\Delta, \qquad \kappa = B_2\Delta, \qquad \gamma = B_3\Delta, \tag{8}$$

where B_1, B_2 and B_3 are the strain displacement relations and Δ are the displacements. The thermo-mechanical finite element model is given by:

$$[K^{\mathrm{e}}]\{\Delta^{\mathrm{e}}\} = \{F^{\mathrm{e}}\} + \{F_T^{\mathrm{e}}\}, \tag{9}$$

where

$$[K^{\mathrm{e}}] = \iint (B_1^T A B_1 + B_1^T B B_2 + B_2^T B B_1 + B_2^T D B_2 + B_3^T S B_3)\,\mathrm{d}\,(\mathrm{Area}),$$

$$\{\Delta^{\mathrm{e}}\} = \{\{u\} \quad \{v\} \quad \{w\} \quad \{\phi_1\} \quad \{\phi_2\}\}^{\mathrm{T}},$$

$$\{F^{\mathrm{e}}\} = \iint (B_1^T N + B_2^T M)\,\mathrm{d}\,(\mathrm{Area}),$$

$$\{F_T^{\mathrm{e}}\} = \iint (B_1^T N^T + B_2^T M^T)\,\mathrm{d}\,(\mathrm{Area}).$$

For any given mechanical and temperature loadings, equation (9) can be assembled and solved to determine displacements and stresses.

3. Composite Failure Model

Tsai–Wu failure criterion is used here for failure evaluation of hydrogen composite storage cylinders [16]. Taking 1 as fiber direction, 2 as transverse direction and 3 as through-the-thickness direction, Tsai–Wu failure criterion can be expressed as:

$$\begin{aligned} I_F = {} & F_1\sigma_{11} + F_2\sigma_{22} + F_{11}\sigma_{11}^2 + F_{22}\sigma_{22}^2 + F_{44}\sigma_{23}^2 \\ & + F_{55}\sigma_{13}^2 + F_{66}\sigma_{12}^2 + 2F_{12}\sigma_{11}\sigma_{22} < 1.0. \end{aligned} \tag{10}$$

The coefficients in equation (10) are defined as:

$$F_1 = \frac{1}{X_{\mathrm{t}}} + \frac{1}{X_{\mathrm{c}}}, \qquad F_2 = \frac{1}{Y_{\mathrm{t}}} + \frac{1}{Y_{\mathrm{c}}}, \qquad F_{11} = -\frac{1}{X_{\mathrm{t}}X_{\mathrm{c}}},$$

$$F_{22} = -\frac{1}{Y_{\mathrm{t}}Y_{\mathrm{c}}}, \qquad F_{44} = \frac{1}{S_{23}^2}, \qquad F_{55} = \frac{1}{S_{13}^2}, \qquad F_{66} = \frac{1}{S_{12}^2},$$

$$F_{12} = \frac{1}{2\sigma_{\text{biax}}^2}\left[1 - \left(\frac{1}{X_\text{t}} + \frac{1}{X_\text{c}} + \frac{1}{Y_\text{t}} + \frac{1}{Y_\text{c}}\right)\sigma_{\text{biax}} + \left(\frac{1}{X_\text{t}X_\text{c}} + \frac{1}{Y_\text{t}Y_\text{c}}\right)\sigma_{\text{biax}}^2\right]$$

or

$$F_{12} = f\sqrt{F_{11}F_{22}} \quad (-1 \leqslant f \leqslant 1),$$

where X_t and X_c are tensile and compressive strengths along fiber direction, Y_t and Y_c are tensile and compressive strengths in transverse fiber direction, S_{23}, S_{13} and S_{12} are the maximum shear strength in corresponding planes, σ_{biax} is the equi-biaxial stress at failure and f is an experience coefficient.

4. Material Properties

Mechanical and thermal properties of fiber reinforced composites vary significantly with temperature. As the carbon/epoxy laminate carries the pressure loading, the effect of temperature on its material properties cannot be ignored. The moduli and thermal expansion coefficients are dependent on temperature. For HFG CU125 carbon/epoxy, in the temperature range $25^\circ\text{C} < T < 140^\circ\text{C}$, the temperature dependent material properties are given by [17]:

$$\begin{aligned}
E_1 &= -0.066T + 128 \text{ (GPa)},\\
E_2 &= -0.064T + 10.67 \text{ (GPa)},\\
G_{12} &= -0.034T + 5.39 \text{ (GPa)},\\
\upsilon_{12} &= -0.0005T + 0.44,\\
\alpha_1 &= (0.0003T^2 - 0.04T + 2.09) \times 10^{-6},\\
\alpha_2 &= (0.0041T^2 - 0.23T + 32.2) \times 10^{-6} \quad (25^\circ\text{C} < T < 140^\circ\text{C}).
\end{aligned} \tag{11}$$

Furthermore, it is assumed that $G_{13} = G_{12}$ and $G_{23} = 0.7G_{12}$. The ultimate strengths of carbon/epoxy do not change much within this temperature range and are assumed to be constant and are listed in Table 1. The material properties for glass/epoxy are listed in Table 2. The outer most glass/epoxy layer is primarily used for protection of the load bearing carbon/epoxy lamina. Hence temperature dependent material properties are not used for the glass/epoxy layers. Properties of innermost aluminum liner are listed in Table 3.

Table 1.
Ultimate strength of carbon/epoxy composite

Strength (MPa)	F_L^t	F_L^c	F_T^t	F_T^c	F_{LT}^S
	1070	1070	40	170	70

Table 2.
Mechanical and thermal properties of S-glass/epoxy

E_1 (GPa)	E_2 (GPa)	$G_{12} = G_{13}$ (GPa)	G_{23} (GPa)	υ_{12}	α_1 (1/°C)	α_2 (1/°C)
55	16	7.6	5.0	0.28	6.3×10^{-6}	32×10^{-6}
Strength	F_L^t	F_L^c	F_T^t	F_T^c	F_{LT}^S	
(MPa)	1620	690	40	140	60	

Table 3.
Mechanical and thermal properties of aluminum 6061-T6

Elastic modulus, E (GPa)	Poisson's ratio, υ	Yield strength, σ_y (MPa)	α (1/°C)
70	0.33	455	24.3×10^{-6}

5. Finite Element Simulation

ABAQUS is an integrated and open-ended finite element analysis code which is widely used by the industry as well as researchers due to its flexibility of implementing user defined subroutines and its powerful nonlinear solver. All the modeling features described in this work have been implemented in this code through user subroutines. A laminated shell element, based on doubly curved shell theory, accounting for membrane, bending, membrane–bending coupling, and transverse shear effects, is suitable for modeling both thin and thick laminated composite. Hence, the laminated composite wall of the cylinder is modeled using doubly curved 8-nodes shell element S8R. In order to estimate the failure pressure of the cylinder, it is necessary to include failure criterion. Tsai–Wu failure theory is utilized to check and report the ply-by-ply laminate failure by using the user subroutine UVARM. In addition, the temperature dependent material properties are incorporated in the model by using the subroutine USDFLD so that, at each integration point, the material properties are determined by the given temperature. The orientation of each element at every ply is handled by the subroutine ORIENT according to winding pattern. The comprehensive model is then solved by using ABAQUS/standard solver accounting for geometric nonlinearity. The cylinder is modeled and meshed using ABAQUS/CAE preprocessor (Fig. 3). Due to the symmetry, only 1/8th of the cylinder is considered for the analysis.

The dimensions considered in the present cylinder analysis are based on a typical design from literature [15]. The outer radius of the cylinder is taken as $R_{\text{out}} = 0.47$ m and inner radius $R_{\text{in}} = 0.44$ m (Fig. 1). The pressure bearing carbon/epoxy laminate consists of 24 plies with a composite shell of thickness 28 mm. The protective glass/epoxy layer and liner are 2 mm and 2.5 mm thick, respectively.

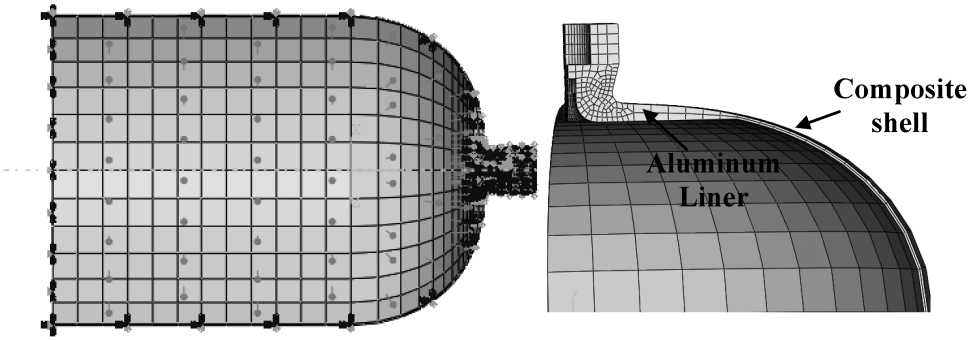

Figure 3. Finite element model of hydrogen cylinder.

The cylinder is subjected to a gradually increasing internal pressure until first ply failure occurs.

To manufacture closed cylinders, two types of winding patterns are usually used: hoop and helical/polar windings. The thickness ratio R (total thickness of helical laminate/total thickness of hoop laminate) affects the failure pressure of the cylinder and a range of 0.1 to 2.0 is studied. Winding angle of laminae also affects the failure pressure of the cylinder and a range of 10° to 30° for helical winding and 89° for hoop winding has been considered based on the manufacturing feasibility. The plies in the protective glass/epoxy laminate are oriented at ±45°.

6. Neural Network Model

Feedforward back-propagation neural network (NNk) is used to predict the failure pressure of hydrogen cylinder. The schematic of the NNk is shown in Fig. 4. The relation between the failure pressure and the NNk inputs (thickness ratio R, temperature inside the cylinder T_{in}, temperature outside the cylinder T_{out} and winding angle θ) is modeled by a two-layer (hidden layer and output layer) network. Each layer consists of a number of processing units, with an activation function, known as neurons. For faster training and robust NNk, inputs are scaled to a desirable range by a designed transfer function f_{in}^{T} before entering the input layer. Inputs are passed through weighted connections to the hidden layer and then to the output layer. The output P' is, finally, scaled back to failure pressure P by a designed transfer function $f_{\text{out}}^{\text{T}}$. The number of neurons in the hidden layer and characterizing weights and biases in the model are determined by training the NNk. Input transfer function for the NNk model is given by:

$$f_{\text{in}}^{\text{T}}(I_i) = I_i \cdot a_i + b_i, \tag{12}$$

where I_i are input variables ($i = 1, 2, 3$ and 4 corresponding to R, T_{in}, T_{out} and θ, respectively), $a_i = (n_{\max} - n_{\min})/(\vec{I}_i^{\max} - \vec{I}_i^{\min})$, $b_i = n_{\min} - \text{Min}\{a_i \cdot \vec{I}_i\}$, $[n_{\min}\ \ n_{\max}]$ is the desired scale range and is taken as $[-1\ \ 1]$ and $\vec{I}_i$ are input training pattern vectors.

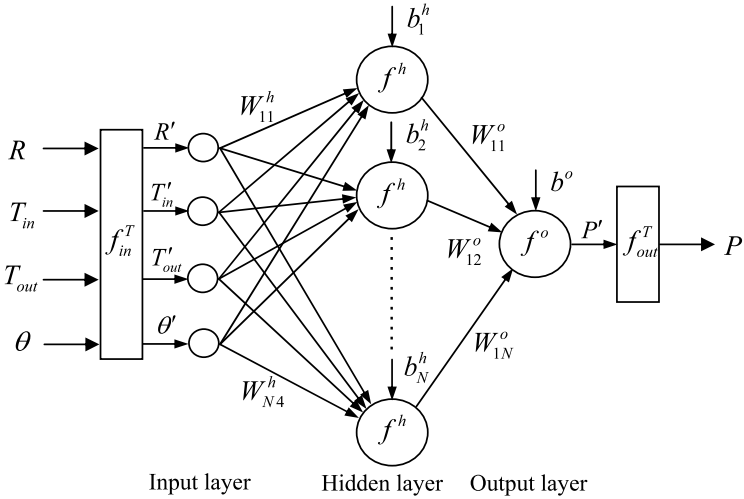

Figure 4. Feedforward back-propagation neural network architecture.

The normalized input variables I'_i are given by

$$I'_i = f_{\text{in}}^{\text{T}}(I_i). \tag{13}$$

The activation function in the hidden layer is the log-sigmoid function

$$f^{\text{h}}(x) = \frac{1}{1+e^{-x}}. \tag{14}$$

The activation function in the output layer is the Pureline function

$$f^{\text{o}}(x) = x. \tag{15}$$

The normalized failure pressure P' is given by:

$$P' = \sum_{j=1}^{N} W_{1j}^{\text{o}} f^{\text{h}}\left(\sum_{i=1}^{4} W_{ji}^{\text{h}} I'_i + b_j^{\text{h}}\right) + b^{\text{o}}, \tag{16}$$

where N is number of neurons in the hidden layer, W_{1j}^{o} are weights in the output layer, W_{ji}^{h} are weights in the hidden layer, b^{o} is bias in the output layer and b_j^{h} are biases in the hidden layer. The output transfer function for the NNk is given by:

$$f_{\text{out}}^{\text{T}}(I_i) = \frac{P' - b}{a}, \tag{17}$$

where

$$a = \frac{n_{\max} - n_{\min}}{\vec{P}^{\max} - \vec{P}^{\min}}, \quad i = 1, 2, 3 \text{ and } 4,$$

$$b = n_{\min} - \text{Min}\{a_u \cdot \vec{P}\}, \quad i = 1, 2, 3 \text{ and } 4,$$

and $\vec{P}$ is the output training pattern vector.

The final failure pressure P is given by

$$P = f_{\text{out}}^{\text{T}}(P'). \tag{18}$$

Training consists of providing a set of known input–output pairs (or patterns) to the network. The back-propagation learning process has two passes through the network: a forward calculation pass and an error back-propagation pass. In the forward pass, input patterns broadcast from input layer to output layer in order to generate the actual results of network. During the backward propagation, weights in each node are iteratively adjusted based on the errors using the gradient descent equations. The procedure is repeated until convergence is achieved. In this study, the input–output sets are obtained from simulation results. The model is trained in MATLAB NNk toolbox. The Levenberg–Marquardt algorithm is adopted in the training process due to its fast convergence.

7. Results and Discussion

Five configurations of helical and hoop laminas shown in Table 4 are investigated in this study. Case studies are conducted on composite cylinders with various thermal loadings and lay-up patterns. Failure pressures as a function of thickness ratio R under uniform thermal loadings for Cases 1–3 are shown in Fig. 5a–5c, respectively. The rate of increase in failure pressure is higher at higher temperatures. This reflects the nonlinearity of thermal expansion coefficients with variation in temperature. For all the three cases considered, the failure pressure increases with increase in temperature. In comparison with Cases 2 and 3, the peak failure pressure is slightly higher than that of Case 1. Similar results are shown in Fig. 6a–6c with gradient thermal loading. The peak failure pressure is not evident for some of the inner temperatures considered in Fig. 6a. In those cases, all hoop laminae are placed over helical laminae with inner temperature higher than outer temperature. Then thermal strain, arising from thermal expansion, becomes larger in all helical laminae which cause

Table 4.
Lay-up configurations for various winding patterns

Case No.	Lay-up pattern
1	$[\pm 20^\circ]_{3s}/[\pm 89^\circ]_{3s}$
2	$[\pm 20^\circ/\pm 89^\circ]_6$
3	$[\pm 10^\circ/\pm 89^\circ/\pm 14^\circ/\pm 89^\circ/\pm 18^\circ/\pm 89^\circ/\pm 22^\circ/\pm 89^\circ/\pm 26^\circ/\pm 89^\circ/\pm 30^\circ/\pm 89^\circ]$
4	$[\pm 10^\circ/\pm 89^\circ]_6$
5	$[\pm 30^\circ/\pm 89^\circ]_6$

Description:
24 layers with total thickness of 28 mm,
$T_{\text{in}} = [25, 50, 75, 100, 120, 140]^\circ\text{C}$,
$T_{\text{out}} = [25, 50, 75, 100, 120, 140]^\circ\text{C}$.

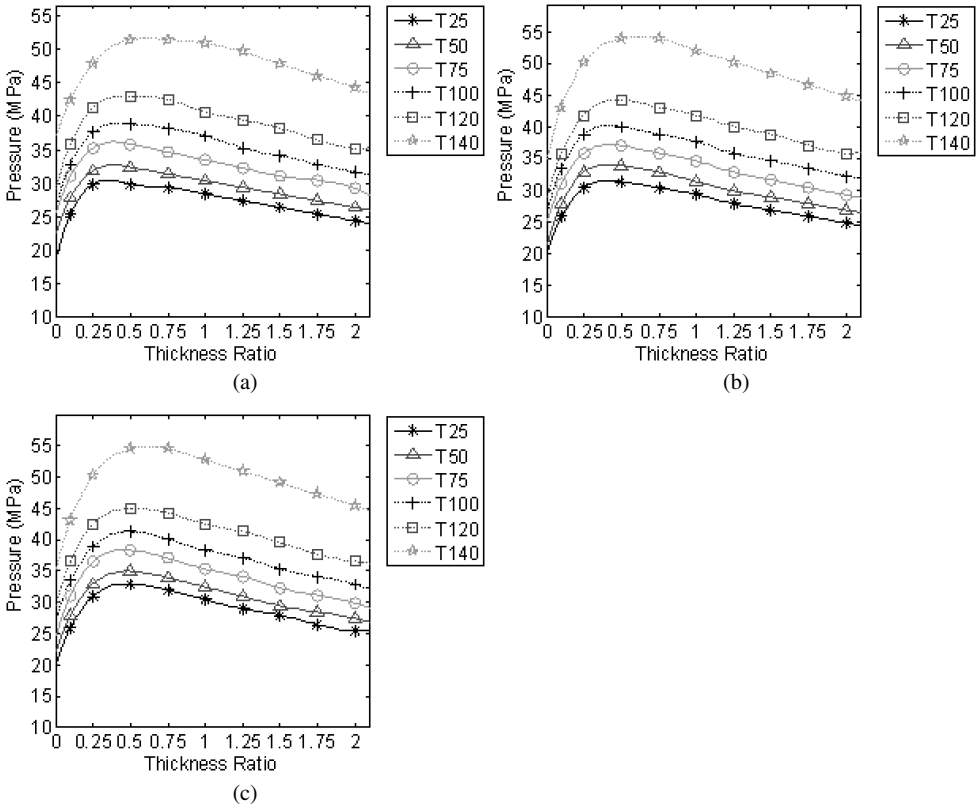

Figure 5. Uniform thermal loading with $T_{in} = T_{out}$ (in (a) Case 1, (b) Case 2 and (c) Case 3).

hoop laminae to carry most of the axial loading. Without helical laminae sustaining the major part of the axial loading, the peak pressure disappears at lower thickness ratio. With increasing thickness ratio, the axial-load bearing capacity of the hoop laminae increases thus resulting in the rise in failure pressure. This phenomenon cannot be observed in Fig. 6b and 6c because the helical and hoop laminae are laid alternately. From Fig. 6a–c, with inner temperature increasing (from 25°C to 140°C), the failure pressure rises till it reaches the set temperature (50°C) of outside wall, and then starts to decrease. Also, it can be observed that the failure pressure decreases as the gradient of the non-uniform temperature increases.

By comparison of Cases 1, 2 and 3, the alternate lay-up pattern (in Cases 2 and 3) results in higher failure pressure than that of non-alternate lay-up (in Case 1), when the cylinder is experiencing uniform thermal loading (Fig. 5). No significant increase in maximum failure pressure is observed in gradient thermal loading. However, in Case 1, the location of peak pressure varies considerably in comparison with that of Cases 2 and 3 under gradient thermal loading. This large variation can bring down the failure pressure at optimum thickness ratio when considering various thermal loads in design. No significant difference is observed between

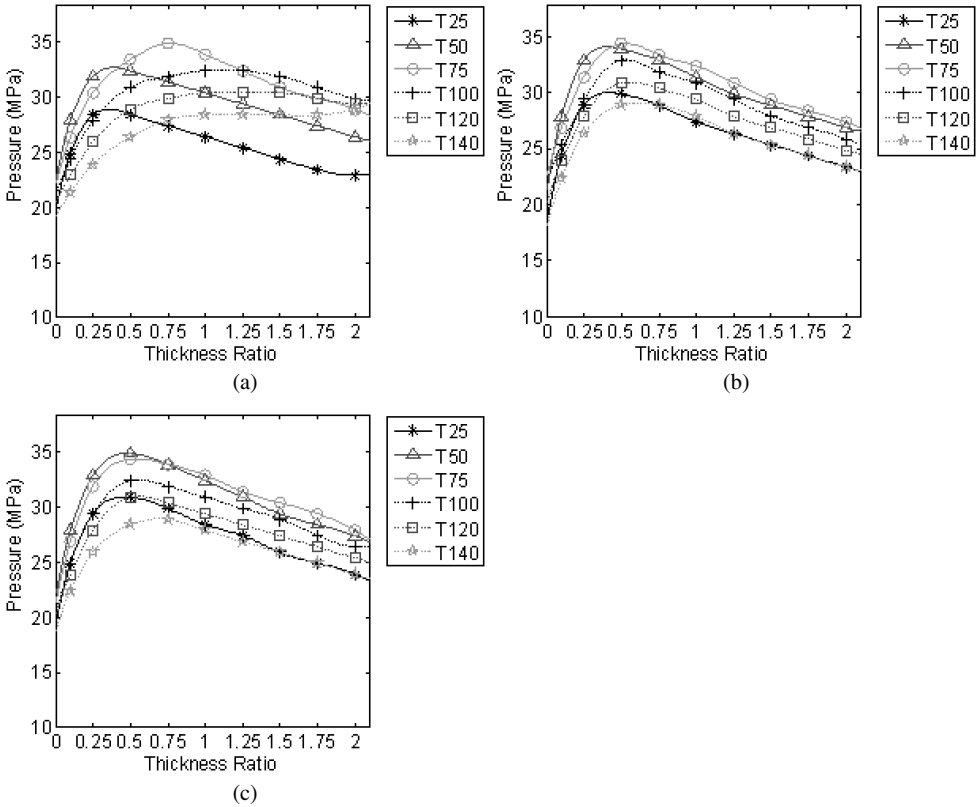

Figure 6. Gradient thermal loading with $T_{out} = 50°C$ (in (a) Case 1, (b) Case 2 and (c) Case 3).

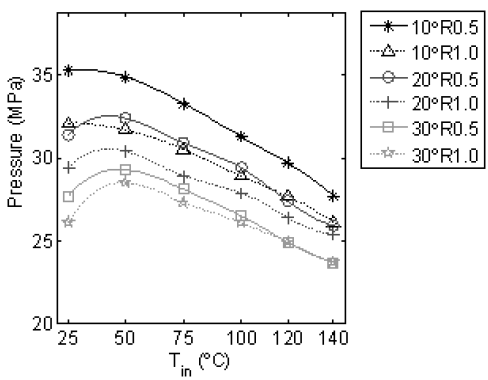

Figure 7. Failure pressure with inside temperature variation ($T_{out} = 25°C$).

Case 2 (constant winding angle in helical laminate) and Case 3 (gradually increased winding angle in helical laminate). To study the effect of helical winding angle pattern on failure pressure, Cases 2, 4 and 5 ($[\pm 20°/\pm 89°]_6$, $[\pm 10°/\pm 89°]_6$ and $[\pm 30°/\pm 89°]_6$) are compared for different thickness ratios (R) as shown in Fig. 7.

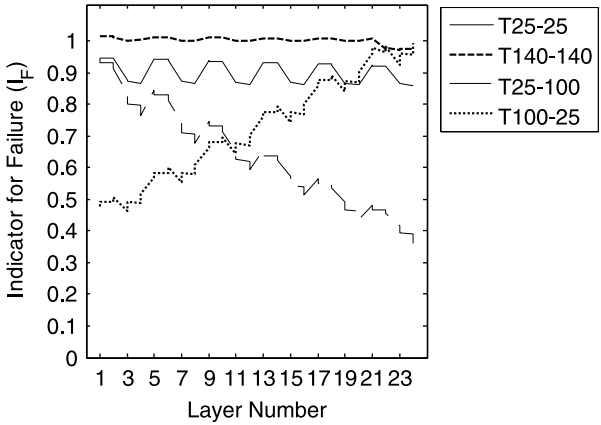

Figure 8. Ply-by-ply failure predictions under various thermal loadings.

For the same thickness ratio, higher peak failure pressure is observed for smaller winding angle.

Figure 8 shows the Tsai–Wu failure indicator for each helical and hoop ply in Case 2 for thickness ratio, $R = 0.5$. Curves 1 and 2 (T25-25 and T140-140, respectively) illustrate the ply failure under uniform thermal loadings while curves 3 and 4 (T25-100 and T100-25, respectively) show the failure under gradient thermal loading (T25-25 implies $T_{\text{in}} = 25°\text{C}$ and $T_{\text{out}} = 25°\text{C}$). With uniform thermal loading at 140°C, the curve is observed to be flat, which implies that all the helical and hoop laminae fail simultaneously. However, at uniform thermal loading of 25°C the helical laminae tend to fail first. When subjected to non-uniform thermal loading, a large slope is observed in the curves. The inner layers fail first for T25-100 ($T_{\text{in}} = 25°\text{C}$ and $T_{\text{out}} = 100°\text{C}$), while the outer layers fail for T100-25 ($T_{\text{in}} = 100°\text{C}$ and $T_{\text{out}} = 25°\text{C}$). This asynchronous behavior of inner or outer layers during failure causes a significant drop in maximum failure pressure, assuming that the cylinder fails when any one of the laminae fails.

The network is trained by using the simulation results from Cases 2, 4 and 5 shown in Table 4. There are 12 neurons used in the neural network (NNk) model and the training ratio is set to 0.01. After the convergence of the network, the model parameters are obtained and are listed in Tables 5 and 6. The network model is then capable of predicting the failure pressure by providing the network inputs (R, T_{in}, T_{out} and θ). To evaluate the performance of NNk prediction, six test cases (shown in Table 7) are studied. The test data from ABAQUS simulation results, for winding angles not used before (15° and 25°), are used to compare the predicted results from the trained neural network. The performance of the NNk is then illustrated in Fig. 9a and 9b, and the maximum errors are reported for each case in Table 7. It can be seen that the results predicted by NNk model are in good agreement with the

Table 5.
Weights and biases for trained neural network

j	Weights in hidden layer				Weights in output layer, W^{o}_{1j}	Biases	
	W^{h}_{j1}	W^{h}_{j2}	W^{h}_{j3}	W^{h}_{j4}		b^{h}_{j}	b^{o}
1	−1.0803	0.1725	1.7439	−0.3099	54.4500	−6.1185	76.6459
2	0.3894	−0.2582	0.1213	0.5764	−123.692	3.6584	
3	−0.4838	0.3915	−0.1974	−0.8114	−36.1329	−3.0100	
4	0.0004	−1.4978	3.5075	0.0280	26.9054	−3.3369	
5	−0.0197	−1.8098	3.9087	0.0127	−19.1409	−3.1452	
6	−8.3694	1.6462	−1.4688	0.0064	−0.3018	−7.8153	
7	−0.3793	0.6444	−0.6923	−0.7765	−1.7120	−0.0646	
8	−1.4274	3.7237	11.3865	0.3180	45.0033	−4.3089	
9	−0.4287	11.4817	−10.7445	−0.6810	0.3312	1.5414	
10	11.3451	−0.0102	0.3561	0.8548	0.6626	11.8876	
11	−1.7027	0.2808	1.7533	−0.2670	−46.5796	−6.7410	
12	1.4200	−3.7174	−11.3598	−0.3166	45.1670	4.3021	

Table 6.
Scaling constants for trained neural network

i	a_i	b_i	a	b
1	1.05263	−1.10526	0.05090	−1.96068
2	0.01739	−1.43478		
3	0.01739	−1.43478		
4	0.10000	−2.00000		

Table 7.
Test cases and maximum error of prediction

Testing case	Inputs			Max. error (%)
	T_{in} (°C)	T_{out} (°C)	θ (°)	
1	40	40	15	1.32
2	30	80	15	−1.54
3	130	40	15	1.23
4	40	40	25	1.11
5	30	80	25	−2.40
6	130	40	25	−1.00

simulation results. The trained network can, therefore, be used to predict any failure pressure within the trained ranges of temperature, winding angle and thickness ratio.

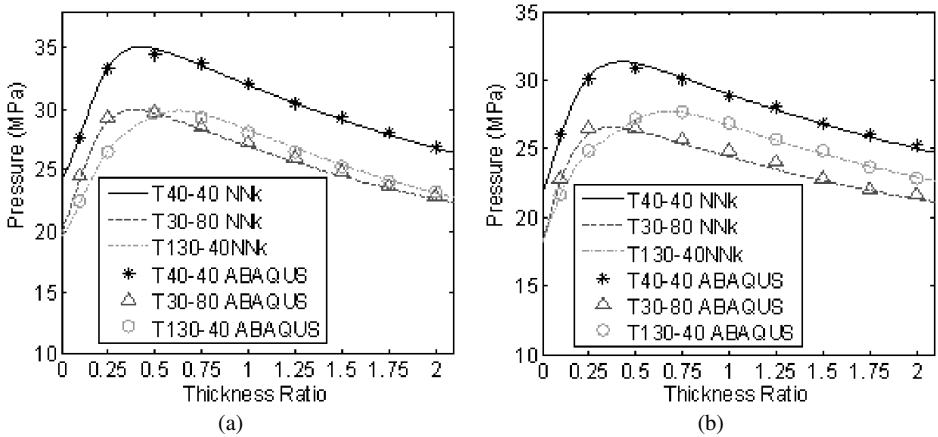

Figure 9. Comparison of failure pressures from NNk and ABAQUS at (a) $\theta = 15°$ and (b) $\theta = 25°$.

8. Conclusions

A doubly curved shell model accounting for transverse shear deformation is used for thermo-mechanical analysis of composite hydrogen storage cylinders. Temperature dependent material properties of the load carrying carbon/epoxy layer and geometry nonlinearity are also considered in the numerical model. Five typical cases have been considered and the analysis is carried out by applying uniform/non-uniform thermal loading and internal pressure loading. The Tsai–Wu failure criterion is employed to predict the failure pressure by checking the failure layer by layer. Under uniform thermal loading, a temperature increase significantly increases maximum failure pressure. In contrast, the non-uniform thermal loading can cause an uneven load distribution and hence decrease the maximum failure pressure. The thickness ratio also plays an important role in determining the maximum failure pressure and should be selected appropriately based on the thermal and mechanical loading conditions. A neural network (NNk) model is developed and used to predict the failure pressure. The performance of the trained neural network is then evaluated by comparing the predicted values with those of test cases and the results are in good agreement.

Acknowledgement

This project is funded by National University Transportation Center.

References

1. N. Takeichia, H. Senoha, T. Yokotab, H. Tsurutab, K. Hamadab, H. Takeshitac, H. Tanakaa, T. Kiyobayashia, T. Takanod and N. Kuriyamaa, Hybrid hydrogen storage vessel, a novel high-pressure hydrogen storage vessel combined with hydrogen storage material, *Intl J. Hydrogen Energy* **28**, 1121–1129 (2003).

2. C. Liang, H. Chen and C. Wang, Optimum design of dome contour for filament-wound composite pressure vessels based on a shape factor, *Compos. Struct*. **58**, 469–482 (2002).
3. V. V. Vasiliev, A. A. Krikanov and A. F. Razin, New generation of filament-wound composite pressure vessels for commercial applications, *Compos. Struct*. **62**, 449–459 (2003).
4. P. Y. Tabakov and E. B. Summers, Lay-up optimization of multilayered anisotropic cylinders based on a 3-D elasticity solution, *Comput. Struct.* **84**, 374–384 (2006).
5. J. Park, C. Hong, C. G. Kim and C. U. Kim, Analysis of filament wound composite structures considering the change of winding angles through the thickness direction, *Compos. Struct*. **55**, 63–71 (2002).
6. S. Kobayashi, T. Imai and S. Wakayama, Burst strength evaluation of the FW-CFRP hybrid composite pipes considering plastic deformation of the liner, *Composites Part A* **38**, 1344–1353 (2007).
7. M. Z. Kabir, Finite element analysis of composite pressure vessels with a load sharing metallic liner, *Compos. Struct*. **49**, 247–255 (2000).
8. D. L. Gray and D. J. Moser, Finite element analysis of a composite overwrapped pressure vessel, in: *40th AIAA/ASME/SAE/ASEE Joint Propulsion Conference and Exhibit*, Fort Lauderdale, FL, USA, AIAA 2004–3506, pp. 1–15, July 11–14 (2004).
9. I. H. Akcay and I. Kaynak, Analysis of multilayered composite cylinders under thermal loading, *J. Reinf. Plast. Compos*. **24**, 1169–1179 (2005).
10. O. Sayman, Analysis of multi-layered composite cylinders under hygrothermal loading, *Composites Part A* **36**, 923–933 (2005).
11. J. M. Schneider, Gaseous hydrogen station test apparatus: verification of hydrogen dispenser performance utilizing vehicle representative test cylinders, in: *SAE World Congress and Exhibition*, Detroit, MI, USA, pp. 1–10, April (2005).
12. J. Hu, J. Chen, S. Sundararaman, K. Chandrashekhara and W. Chernicoff, Analysis of composite hydrogen storage cylinders subjected to localized flame impingements, *Intl J. Hydrogen Energy* **33**, 2738–2746 (2008).
13. K. Chandrashekhara and A. Bhimaraddi, Thermal stress analysis of laminated doubly curved shells using a shear flexible finite element, *Comput. Struct.* **52**, 1023–1030 (1994).
14. K. Chandrashekhara and T. Schroeder, Nonlinear impact analysis of laminated cylindrical and doubly curved shells, *J. Compos. Mater*. **29**, 2160–2179 (1995).
15. F. Mitlitsky, A. H. Weisberg and B. Myers, Vehicular hydrogen storage using lightweight tanks, *Proc. U.S. DOE Hydrogen Prog. Rev*. NREL/CP-570-28890 (2000).
16. S. W. Tsai and E. M. Wu, A general theory of strength for anisotropic materials, *J. Compos. Mater.* **5**, 58–80 (1971).
17. K. J. Yoon and J. Kim, Prediction of thermal expansion properties of carbon/epoxy laminae for temperature variation, *J. Compos. Mater*. **34**, 90–100 (2000).